

# Resolving the Shocks in Radio Galaxy Nebulae: HST and Radio Imaging of 3C 171, 3C 277.3, and PKS 2250-41 <sup>1</sup>

Avanti Tilak<sup>a</sup>, Christopher P. O'Dea<sup>b</sup>, Clive Tadhunter<sup>c</sup>, Karen Willis<sup>c</sup>, Raffaella Morganti<sup>d</sup>, Stefi A. Baum<sup>d</sup>, Anton M. Koekemoer<sup>f</sup>, and Daniele Dallacasa<sup>g,h</sup>

## ABSTRACT

We present the results of HST/WFPC2 medium and narrow band imaging and VLA and MERLIN2 radio imaging of three powerful radio galaxies: 3C 171, 3C 277.3, and PKS 2250-41. We obtained images of the rest frame [OIII] $\lambda$ 5007 and [OII] $\lambda$ 3727 line emission using the Linear Ramp Filters on WFPC2. The correlations between the emission line morphology and the [OIII]/[OII] line ratios with the radio emission seen in ground based observations are clarified by the HST imaging. We confirm that the radio lobes and hot-spots are preferentially associated with lower ionization gas. 3C 171 exhibits high surface brightness emission line gas mainly along the radio source axis. The lowest ionization gas is seen at the Eastern hot spot. In 3C 277.3 there is bright high ionization gas (and continuum) offset just to the east of the radio knot K1. Our observations are consistent with previous work suggesting that this emission is produced by precursor gas ionized by the shock being driven into the cloud by the deflected radio jet. In PKS 2250-41 we resolve the emission line arc which wraps around the outer rim of the western lobe. The lower ionization [OII] emission is nested just interior to the higher ionization [OIII] emission suggesting that we have resolved the cooling region behind the bow shock. We also detect possible continuum emission from the secondary hot-spot. Thus, our observations support the hypothesis that in these sources, the interaction between the expanding radio source and the ambient gas strongly influences the morphology, kinematics, and ionization of the gas.

*Subject headings:* galaxies: active — galaxies: jets — shock waves — galaxies: individual (3C 171, PKS 2250-41, 3C 277.3) — galaxies: interaction — galaxies: kinematics and dynamics

---

<sup>a</sup>Department of Physics & Astronomy, The Johns Hopkins University, 3400 N. Charles Street, Baltimore, MD-21218; tilak@pha.jhu.edu

<sup>b</sup>Department of Physics, Rochester Institute of Technology, One Lomb Memorial Drive, Rochester, NY-14623; odea@cis.rit.edu

<sup>c</sup>Department of Physics & Astronomy, University of Sheffield, Western Bank, Sheffield, S10 2TN, UK; C.Tadhunter@sheffield.ac.uk, K.Willis@sheffield.ac.uk

<sup>d</sup>Netherlands Foundation for Research in Astronomy, Postbus 2, 7990 AA Dwingeloo, The Netherlands; morganti@astron.nl

<sup>e</sup>Center for Imaging Sciences, Rochester Institute of Technology, One Lomb Memorial Drive, Rochester, NY-14623; baum@cis.rit.edu

<sup>f</sup>Space Telescope Science Institute, 3700 San Martin Dr., Baltimore, MD 21218; koekemoer@stsci.edu

<sup>g</sup>Dipartimento di Astronomia, via Ranzani 1, I-40127 Bologna, Italy

<sup>h</sup>Ist. di Radioastronomia, CNR, Via Gobetti 101, I-40129 Bologna, Italy; ddallaca@ira.cnr.it

<sup>1</sup>Based on observations made with the NASA/ESA Hubble Space Telescope, obtained at the Space Telescope Science Institute, which is operated by the Association of Universities for Research in Astronomy, Inc., under NASA contract NAS 5-26555. These observations are associated with program 6657 (PI C. Tadhunter).

<sup>2</sup>Operated by the Association of Universities for Research in Astronomy under contract NAS 5-26555 with the National Aeronautics and Space Administration.

## 1. Introduction

The association of powerful radio galaxies with luminous extended emission line nebulae is well established (e.g., Heckman *et al.* 1982, Meisenheimer & Hippelein 1992, Baum & McCarthy 2000). There has been great debate over whether nuclear photo-ionization or shock heating is the dominant source of ionization. However, it is becoming clear that both mechanisms are present in the extended nebulae, e.g., (Clark *et al.* 1998; Villar-Martín *et al.* 1999; O’Dea *et al.* 2002). In principle it should be possible to use the properties of the shocked gas to study the nature of the jet-cloud interaction and constrain the physics of the propagation of the radio source. Here we present a high resolution HST/WFPC2 imaging study of three powerful radio galaxies in which previous ground based imaging and spectroscopy has revealed the presence of shocked gas in the extended nebula (Clark *et al.* 1997, 1998; Villar-Martín *et al.* 1999; Tadhunter *et al.* 2000; Solorzano-Iñarrea & Tadhunter 2003). We detail the data reduction and analysis techniques in §2. The properties of the sources are summarized in Tables 1 & 2. In §3 we present the results of the emission line imaging and a comparison with the radio source morphology. The results are summarized in §4. Throughout the paper, we have used  $H_0=75 \text{ km s}^{-1}\text{Mpc}^{-1}$  and  $q_0=0.0$ .

## 2. Observations and Data Analysis

### 2.1. Emission Line Images

We observed the redshifted [OIII] $\lambda$ 5007 and [OII] $\lambda$ 3727 emission lines using the HST/WFPC2 Linear Ramp Filters (LRF). The LRF are divided into four parallel strips each with the central wavelength varying across each strip by about 6 percent (Biretta *et al.* 2002). In general for a given wavelength, the effective field of view is about  $13''$ . The object was placed in that part of the chip which corresponds to the desired wavelength. In addition to the narrow-band emission line images taken with the ramp filters, intermediate-band continuum images were taken using the F467M and F547M filters, in order to facilitate accurate continuum subtraction and allow examination of the detailed continuum structures. The central wavelengths and bandwidths of the medium band filters were chosen to avoid bright emission lines. The parameters of the HST observations are given in Table 3.

The data were calibrated with standard software in STSDAS. Due to the fine vignetting of the LRF filters, flats obtained from nearby narrow band filters were used for flat fielding (Biretta, Baggett & Noll 1996). The DRIZZLE algorithm (Fruchter & Hook 2002; Koekemoer 2002) was used for combining dithered images. The algorithm is also very efficient at rejecting cosmic rays. These dithered images were used in the subsequent analysis. The tasks in the SYNPHOT package were used for flux calibration. Adopting an input “average” emission line profile, we used CALCPHOT to estimate the number of counts expected for a Gaussian signal. The characteristics of this input were then used to convert the image from counts to flux units. The photometric calibration of the LRF data should be accurate to  $\sim 3\%$  (Biretta *et al.* 1996).

It was necessary to register the LRF and continuum images using WREGISTER, since the source is not located at the same pixels in these images. This task performs a spatial transformation so that the WCS coordinates of the input image match the coordinates of the reference image at the same logical pixel coordinates. This first shift is good to a few pixels. We then manually shifted by a few pixels to register the nucleus on the images. Our images do not show significant dust, so the location of the nucleus was obvious on the continuum and line images.

We used CALCPHOT to estimate the flux expected through each of the filters for a standard elliptical galaxy template. We used the ratios of the estimated fluxes to scale the medium band image to subtract the continuum contribution from the LRF images. Over much of the extent of the nebulae, the continuum is weak or undetected and the stellar continuum correction to the LRF images ranges from a few percent to less than one percent of the counts in the LRF image. In a few locations, e.g., the nuclei of 3C277.3 and PKS2250-41,

the correction to the LRF image is as large as 10-20%. In principle, there could be a contribution to the continuum from e.g., scattered nuclear light or a young stellar population (e.g., Chambers & Miley 1990). If this were the case, the result could be an increase in the correction to the LRF images, but over most of the nebula the correction is still a small fraction of the counts in the LRF image.

## 2.2. Radio Images

Radio observations images for all three sources were obtained with the VLA in the A configuration. In addition a 36 hour observation on 3C 277.3 was obtained using MERLIN2 (Table 4). Calibration and data reduction was achieved using standard techniques in the NRAO AIPS software. Observations of a bright point source calibrator were used to determine the antenna gains and phases and to place the observations in the radio reference frame with an accuracy of  $\sim 0.1''$ . The flux density scale was determined using observations of 3C286. After calibration, the data were deconvolved using the CLEAN algorithm, and the instrumental gains and phases were further corrected using self-calibration. The VLA and MERLIN2 data for 3C277.3 were combined to produce a final image.

## 2.3. Data Analysis

The average signal for the background for each of the emission line images was obtained. This background level was subtracted from the corresponding images. The emission line images were smoothed with a Gaussian with a FWHM of 2 pixels in order to increase the surface brightness sensitivity. The smoothing also mitigates the consequences of any small errors in the image registration. The pixels with values less than  $3\sigma$  were masked. The masked [OIII] image was divided by the masked [OII], to obtain the ratio image. In pixels where the [OII] flux was masked, but [OIII] was not, we divided the [OIII] flux by the  $3\sigma$  value for the unmasked [OII] image so as to obtain a lower limit on the ratio in those regions.

The optical images were rotated so that they were aligned with the radio images and then the optical and radio nuclei (which are visible on all images) were registered and the images overlayed. We estimate that the radio and optical images are registered to within 1 pixel ( $0.05''$ ). The radio and optical images and various overlays are presented in Figures 1-12.

A small but non-negligible reddening correction (Veilleux & Osterbrock 1987; Osterbrock 1989), was applied for all three galaxies (Table 1). For 3C 171 and PKS 2250-41, the reddening correction includes Galactic as well as internal contributions and was determined using observed  $H\alpha/H\beta$  ratios (Clark *et al.* 1997; Clark *et al.* 1998). For 3C 277.3 the  $H\alpha/H\beta$  and  $H\gamma/H\beta$  measured by Solorzano-Iñarra & Tadhunter (2003), are consistent with Case B suggesting that the reddening is negligible.

# 3. RESULTS

## 3.1. 3C 171

3C 171 is a well studied FR II radio source at redshift of 0.2384 (e.g., Heckman *et al.* 1984, Baum *et al.* 1988, Blundell 1996, Clark *et al.* 1998, Tadhunter *et al.* 2000, Solorzano-Iñarra & Tadhunter 2003). The radio image shows a faint nucleus and two hot-spots and considerable extended diffuse emission which includes large ‘plumes’ which extend roughly perpendicular to the radio lobes (Blundell 1996). Heckman *et al.* (1984) and Baum *et al.* (1988) found that the inner structure of the powerful radio source (within the hotspots) 3C 171 is co-spatial with an extended emission line nebula. Tadhunter *et al.* (2000) obtained deep  $H\alpha$  images which revealed that there is faint diffuse gas extending beyond the radio source and that

the morphology of the emission line gas is closely related to the radio morphology, but does not exhibit the “ionization cone” morphology expected for simple AGN photo-ionization. Long slit (Clark *et al.* 1998) and integral field spectroscopy (Solorzano-Iñarrea & Tadhunter 2003) revealed (1) complex kinematics in the gas including line splitting, and (2) lower ionization gas associated with the hot-spots, and (3) an anti-correlation between line width and ionization state in the gas. Hardcastle (2003) suggested that the depolarization of the radio emission is produced by a warm shocked medium. Taken together, these observations are consistent with the emission line gas having been shocked by the expanding radio source, e.g. Clark *et al.* (1998).

We present our WFPC2 images and radio images in Figures 1-4. Values of the [OIII]/[OII] line ratio are given in Table 6 for selected regions. The medium band continuum image shows some very faint diffuse emission aligned along the radio axis. Comparison of the HST and radio images (Figures 1, 2) shows that the high surface brightness emission line gas tends to follow the central ridge line of the radio source. However, there are some asymmetries in the source. We detect [OIII] but not [OII] above a level of  $4 \times 10^{-18} \text{ ergs s}^{-1} \text{ cm}^{-2} \text{ arcsec}^{-2}$  associated with the Western hot spot (the [OII] emission line gas begins just interior to the hot-spot). However, the lower resolution ground based observations by Solorzano-Iñarrea & Tadhunter (2003) show traces of [OII], [OIII] and  $H\beta$  line emission in this region. On the Eastern side there is [OII] in a band across the hot spot, while the [OIII] extends mainly south of the lobe. We find low ratios of [OIII]/[OII]  $\lesssim 0.5$  associated with the gas near the hot-spots, and higher values  $\sim 1.5 - 2$  about midway between the lobes and the nucleus. The extended structures in this object show a marked similarity with the aligned structures in high redshift radio galaxies.

The lack of any line emission for the western hot-spot is surprising, given that the radio morphology suggests that the jet has hit something there (Blundell 1996). One explanation might be that the shock driven through the warm/cool gas at the western hot-spot may be so strong/fast that the gas is heated to high enough temperatures that the cooling time becomes long (i.e. the gas has not yet cooled to  $\sim 1-2 \times 10^4 \text{ K}$ , so that the optical emission lines become visible).

The anti-correlation between line width and ionization noted by Clark *et al.* (1998) suggests that the compressed, high velocity post-shock gas has a low ionization state, whereas the kinematically quiescent gas has a high ionization state. It is likely that the high surface brightness regions of [OII] emission map the kinematically disturbed post-shock gas, whereas the [OIII] emission is a combination of mostly precursor and some post-shock gas. The striking differences between the emission line structures of the two lines may therefore reflect differences in the spatial distributions of precursor and cooling post-shock gas; in this context it is not surprising that the [OII] is stronger in the eastern lobe than the [OIII], and that [OIII] dominates in the AGN-photoionized nuclear regions.

### 3.2. 3C 277.3 (Coma A)

Coma A is classified as intermediate between FRI and FRII radio galaxies, displaying very broad and diffuse bubble-like lobes. It is relatively nearby with a redshift of 0.0857. Miley *et al.* (1981) first detected optical continuum and emission lines associated with the extended radio lobes. There is an extensive network of emission line filaments which seem to wrap around the radio lobes (van Breugel *et al.* 1985; Tadhunter *et al.* 2000). Van Breugel *et al.* (1985) suggested that the southern jet is deflected by a massive cloud at the location of knot K1. Morganti *et al.* (2002) detect the 21 cm line of HI in absorption against the extended radio lobes of Coma A. They suggest that the source is expanding into a gaseous disk, presumably acquired in a merger which triggered the radio activity. The kinematics of the emission line gas are consistent with interaction with the radio source (van Breugel *et al.* 1985; Solorzano-Iñarrea & Tadhunter 2003).

The HST and radio images are given in Figures 5-8. Values of the [OIII]/[OII] line ratio are given in Table 6 for selected regions. The medium band continuum image shows a very prominent nucleus and the faint continuum emission associated with the northern knot K1 (Fig. 8). The peak of the continuum emission is

shifted just to the east of the radio peak of K1. In our narrow band LRF images we detect the emission line gas associated with the nucleus and the filament which runs mainly N-S and to the East of the two radio knots (Figs. 6, 5). We do not detect any line emission directly associated with knot K2. We see a peak in the line emission just to the east of knot K1. The line emission in this region exceeds that from the nucleus. The observed  $[\text{OIII}]/[\text{OII}]$  ratio also peaks just east of K1 with a relatively high value of  $\sim 5.4$  consistent with the suggestion of Solorzano-Iñarrea & Tadhunter (2003) that the emission lines in this feature are dominated by photoionized precursor emission.

The linear structures visible in the high resolution radio images are very interesting. They are suggestive of shocks that have been driven back into the jets as a consequence of the strong interaction with the emission line cloud. The fact that they are not exactly perpendicular to the jets, but misaligned by  $\sim 30$  degrees to perpendicular, may be significant, since oblique shocks have been proposed as a mechanism for deflecting jets, and the jet is indeed significantly deflected in 3C277.3. The modeling work of Tingay (1997) demonstrates that it is possible to produce a significant deflection for an obliquity of  $\sim 30$  degrees, although as he notes, it may be difficult to produce a deflection as large as that seen in 3C277.3, unless the jet is inclined towards the observer, so that the real jet deflection is less than measured.

The nature of the jet-cloud interaction appears somewhat different to those associated with the other two sources. Whereas in 3C171 and PKS2250-41 the *lowest* ionization features are closely associated with the detailed radio features (knots, hot-spots), in 3C277.3 the highest ionization feature *within the cloud* is closely associated with the radio knot. While this close association – within 0.2 arcseconds in our HST observations – suggests that the jet is ionizing the cloud, it is significant that, unlike the other two sources and also the extended radio lobe in 3C277.3 itself (Solorzano-Iñarrea & Tadhunter 2003), the line emission associated with the jet-knots in 3C277.3 shows no sign of kinematic disturbance. All this is consistent with the idea that, in this case, we are observing pure shock photoionized precursor emission; the shock driven through the warm ISM may be so fast that the shock gas has not yet cooled sufficiently to radiate optical emission lines, or the post shock cloudlets may have been shredded/dispersed by hydrodynamic interaction with the hot post-shock wind before they had a chance to cool (e.g., Klein, McKee & Colella 1994). This may be testable with X-ray observations. However, we cannot entirely rule out the idea the precursor gas in the cloud is photoionized by a narrow blazar beam from the AGN which points exactly in the jet direction; the ionization gradients across the cloud are consistent with this idea provided that the Lorentz factor of the jets close to the nucleus is fairly high (in order to give a narrow beam).

The optical continuum emission associated with the warm emission line cloud is also interesting. Miley *et al.* (1981) detected significant optical polarization ( $14 \pm 3\%$  with a position angle of  $71 \text{ deg} \pm 6 \text{ deg}$ ) that is aligned perpendicular to the radio axis. On the basis of the optical/radio spectral index and polarization they interpreted the optical continuum as synchrotron emission from the same knots that emit the radio emission. However, in this case it is surprising that the continuum emission visible in our HST images appears to be significantly displaced to the east of peak of the high frequency radio emission. On the other hand, the polarization properties of the continuum emission, and its morphological similarity with the  $[\text{OIII}]$  emission, are consistent with the idea that it represents light from the blazar beam of the AGN scattered into our line of sight (very similar to PKS2152-69: see Tadhunter *et al.* 1988, di Serego Alighieri *et al.* 1988). This would also support the idea that the cloud is photoionized by the blazar beam.

### 3.3. PKS 2250-41

PKS 2250-41 is a FRII source at a redshift of 0.308. The first detailed observations by (Tadhunter *et al.* 1994) showed large scale emission line arcs or filaments associated with the radio lobes. Both the kinematics and the ionization of the gas appear consistent with a scenario in which the radio source is interacting with the emission line gas (Clark *et al.* 1997; Villar-Martín *et al.* 1999). Clark *et al.* (1997) find that the radio emis-

sion from the western lobe has very low polarization consistent with depolarization by surrounding/mixed gas.

Our 15 GHz VLA observations resolve structure in the lobes and reveal evidence for secondary hot-spots (e.g., Fig. 9). We also (just) detect the nucleus in the radio which allows improved registration of the optical and radio images.

The HST and radio images are given in Figures 9-12. Values of the [OIII]/[OII] line ratio are given in Table 6 for selected regions. Note that unfortunately the location of the redshifted wavelength of the [OII] line on the LRF lies close to the edge of the chip. Thus, the coverage of the [OII] line does not include the Eastern lobe. This may not be significant as ground based imaging by Clark *et al.* (1997) does not show any emission line gas associated with this lobe.

Our LRF images show line emission from the nuclear region and from the bright filament which points toward the companion galaxy to the north-east. There is also a hint of much more diffuse line emission which is not well detected in these observations. As noted by Tadhunter *et al.* (1994), the emission line gas in the Western lobe takes the form of an arc which wraps around the outer boundary of the lobe (Fig. 10). The [OIII] extends in a roughly 180° semi circle around the front side of the lobe. The [OII] is somewhat smaller in extent and is concentrated closer to the source axis and appears “nested” within the [OIII] arc. The [OII] emission from this ‘nested’ region exceeds that from the nucleus. The [OIII]/[OII] ratio in the lobe is low ( $\lesssim 0.5$ ) and is somewhat higher at the leading edge of the lobe and declines slightly with distance inwards towards the nucleus.

The differences between the detailed [OIII] and [OII] emission line morphologies in the lobe can be explained in terms of different proportional contributions of precursor, AGN-photoionized, and lower ionization, kinematically-disturbed post-shock gas, with AGN photoionization dominating close to the nucleus, shock (photo)ionization of the precursor emission dominating in the extended arc, and cooling post-shock gas dominating the [OII] emission in the lobe. This is consistent with the interpretation of Clark *et al.* (1997) and Villar-Martín *et al.* (1999).

The medium band continuum image shows a possible companion galaxy to the north (Clark *et al.* 1997) and emission associated with the secondary hot-spot in the western lobe. A spur of the continuum emission appears to point toward the companion while the companion itself is elongated in the direction of the nucleus. The position angles of the spur in the continuum, appears to be aligned with the major axis of the companion to within 6 degrees. The alignment is even better between the PA for the major axis of the companion and the filament of PKS2250-41. Table 5 summarizes the position angles of each of the distinctive features of the companion and PKS2250-41. Recent VLT observations of the putative companion galaxy show Balmer absorption lines at the same redshift as PKS2250-41 indicating that it is indeed a companion in the same group and that it has had recent star formation (Tadhunter, in preparation).

The spatial coincidence between the optical continuum emission and secondary hot-spot in the western lobe is striking. One possibility is that the secondary hot-spot in fact represents compact radio emission from the nucleus of a companion galaxy that the jet is colliding with (consistent with the jet-galaxy collision idea presented in Clark *et al.* 1997). In this case, the optical light represents the stellar light of the bulge of this companion galaxy to the west. Alternatively, both the optical and radio emission might be explained in terms of synchrotron emission from the secondary hot-spot. However this possibility is ruled out as a dominant source of emission, due to the lack of optical polarization ( $\lesssim 4.5\%$ , see Shaw *et al.* 1995).

The highly collimated nature of the emission line structure in the nuclear region is reminiscent of the structures aligned along the radio axis in high redshift radio galaxies (Best *et al.* 2000), yet in this case the structure is misaligned from the radio axis by 25 degrees. While radio and optical structures in high  $z$  radio galaxies are rarely in perfect alignment, a deviation of this size is seen in less than 25% of powerful radio sources studied by Chambers, Miley & van Breugel (1987). Moreover, in contrast to the high- $z$  objects, the

emission line kinematics of the linear structure are quiescent. However, the fact that this structure points towards the north-eastern companion (and the companion points towards it!), suggests that the gas has been captured in an interaction with the companion, and that the linear structure is a result of this interaction (perhaps a disk of captured gas seen edge on). In contrast, on the western side of the nucleus in PKS2250-41 the jets are likely to be directly interacting with the debris of the other companion galaxy. Therefore one can interpret PKS2250-41 as a complex system in which the dominant galaxy is interacting with two companions, and the jet is ploughing into the debris of the companion on the west side of the nucleus.

#### 4. CONCLUSIONS

The HST imaging results presented in this paper demonstrate the full diversity of jet-cloud interaction phenomenon, with structures ranging from the bow-shock-like structure that cocoons the western radio lobe in PKS2250-41, to the linear structures closely aligned along the radio axis in 3C171, to the bright emission line cloud associated with the knot along the radio jet in 3C277.3. Amongst low/intermediate redshift radio galaxies PKS2250-41, 3C277.3 and 3C171 are unusual in the strengths of their jet-cloud interactions. In addition, PKS2250-41 and 3C171 have close companions aligned along their radio jets while 3C277.3 shows evidence of a recent merger in which the disk of the debris is observed face-on. It is likely that these objects represent the few rare cases in which the jets are ploughing into the debris left over from the merger events that triggered the activity.

Significant differences are seen between the [OII] and [OIII] structures in all three objects. All of these differences can be explained in terms of varying contributions of cooling post-shock gas, shock photoionized precursor gas, and AGN photoionized gas. The correlations between the emission line morphology and the [OIII]/[OII] line ratios with the radio emission seen in ground based observations are clarified by the HST imaging. We confirm that the radio lobes and hot-spots are preferentially associated with lower ionization gas. 3C 171 exhibits high surface brightness emission line gas mainly along the radio source axis. The lowest ionization gas is seen at the Eastern hot spot. In 3C 277.3 there is bright high ionization gas (and continuum) offset just to the east of the radio knot K1. Our observations are consistent with the suggestion of (Solorzano-Iñarra & Tadhunter 2003) that this emission is produced by precursor gas ionized by the shock being driven into the cloud by the deflected radio jet. In PKS 2250-41 we resolve the emission line arc which wraps around the outer rim of the western lobe. The lower ionization [OII] emission is nested just interior to the higher ionization [OIII] emission, suggesting that we have resolved the cooling region behind the bow shock. We also detect possible continuum emission from the secondary hot-spot.

Thus, our observations support the hypothesis that in these sources, the interaction between the expanding radio source and the ambient gas strongly influences the morphology, kinematics, and ionization of the gas.

#### 5. Acknowledgements

Support for program 6657 (PI C. Tadhunter) was provided by NASA through a grant from the Space Telescope Science Institute, which is operated by the Association of Universities for Research in Astronomy, Inc., under NASA contract NAS 5-26555. The National Radio Astronomy Observatory is a facility of the National Science Foundation operated under cooperative agreement by Associated Universities, Inc. MERLIN is operated as a National Facility by the University of Manchester on behalf of the UK Particle Physics and Astronomy Research Council. This research made use of (1) the NASA/IPAC Extragalactic Database(NED) which is operated by the Jet Propulsion Laboratory, California Institute of Technology, under contract with the National Aeronautics and Space Administration; and (2) NASA’s Astrophysics Data System Abstract Service. We thank Shireen Gonzaga for help with the WFPC2 observations and Peter

Thomasson and Tom Muxlow for assistance with the MERLIN2 observations for 3C277.3. Karen Wills acknowledges financial support from PPARC and the Royal Society. We thank the anonymous referee for very detailed and helpful comments.

## REFERENCES

- Baum, S. A., Heckman, T. M., Bridle, A., van Breugel, W. J. M., Miley, G. K., 1988, *ApJS*, 68, 643
- Baum, S. A., & McCarthy, P. J., 2000, *ApJ*, 119, 2634
- Biretta, J., Baggett, S., Noll, K., 1996, Photometric Calibration of WFPC2 Linear Ramp Filter Data in SYNPHOT, WFPC2 Instrument Science Report 96-06.
- Biretta, Lubin., *et al.* 2002, WFPC2 Instrument Handbook, Version 7.0 (Baltimore:STScI)
- Blundell, K. M. 1996, *MNRAS*, 283, 538
- Chambers, K. C., Miley, G. K., van Breugel, W., 1987, *Nature*, 329, 604
- Chambers, K. C., & Miley, G. K., 1990, in ASP Conf. Ser. 10, The Evolution of the Universe of Galaxies, ed. R. G. Kron (San Francisco: ASP), 373
- Clark, N. E., Tadhunter, C. N., Morganti R., Killeen, N. E. B., Fosbury, R. A. E., Hook, R. N., Seibert, J., Shaw, M. A., 1997, *MNRAS*, 286, 558
- Clark, N. E., Axon, D. J., Tadhunter, C. N., Robinson, A., O’Brien, P., 1998, *ApJ*, 494, 546
- de Young, D. S., 2002, The Physics of Extragalactic Radio Sources (University of Chicago Press, Chicago IL)
- di Serego Alighieri, S., Courvoisier, T. J.-L., Fosbury, R. A. E., Tadhunter, C. N., Binette, L., 1988, *Nature*, 334, 591
- Fruchter, A. S., Hook, R. N., 2002, *PASP*, 114, 144
- Hardcastle, M. J., 2003, *MNRAS*, 339, 360
- Heckman, T. M., Miley, G. K., Balick, B., van Breugel, W. J. M., & Butcher, H. R., 1982, *ApJ*, 262, 529
- Heckman, T. M., van Breugel, W. J. M., Miley, G. K., 1984, *ApJ*, 286, 509
- Hunstead, R., W., 1971, *MNRAS*, 152, 277
- Klein, R. I., McKee, C. F., Colella, P., 1994, *ApJ*, 420, 213
- Koekemoer, A., *et al.* “HST Dither Handbook”, Version 2.0 (Baltimore:STScI)
- McCarthy, P. J., van Breugel, W. J. M., Spinrad, H., Djorgovski, S., 1987, *ApJ*, 321, L29
- Meisenheimer, K. & Hippelein, H., 1992, *A&A*, 264, 455
- Miley, G. K., Heckman, T. M., Butcher, H. R., van Breugel, W. J. M., 1981, *ApJ*, 247, L5
- Morganti, R., Killeen, N. E. B., Tadhunter, C. N., 1993, *MNRAS*, 263, 1023
- Morganti, R., Oosterloo, T. A., Tinti, S., Tadhunter, C. N., Wills, K. A., van Moorsel, G., 2002, *A&A*, 387, 830

- O’Dea, C. P., De Vries, W. H., Koekemoer, A. M., Baum, S. A., Morganti, R., Fanti, R., Capetti, A., Tadhunter, C. N., Barthel, P. D., Axon, D. J., Gelderman, R., 2002, *AJ*, 123, 2333
- Osterbrock, D. E., 1989, *Astrophysics of Gaseous Nebulae and Active Galactic Nuclei*, University Science Books, Mill Valley CA
- Raymond, J. C., 1979, *ApJS*, 39, 1
- Shaw, M., Tadhunter, C. N., Dickson, R., Morganti, R., 1995, *MNRAS*, 275, 703
- Shull, J. M., McKee, C. F., 1979, *ApJ*, 227, 131
- Solorzano-Iñarrea, C., Tadhunter, C. N., 2003, *MNRAS*, 348, 705
- Spinrad, H., Marr, J., Aguilar, L., Djorgovski, S., 1985, *PASP*, 97, 932
- Tadhunter, C. N., Fosbury, R. A. E., di Serego Alighieri, S., Bland, J., Danziger, I. J., Goss, W. M., McAdam, W. B., Snijders, M. A. J., 1988, *MNRAS*, 235, 403
- Tadhunter, C. N., Shaw, M., Clark, N. E., Morganti, R., 1994, *A&A*, 288L, 21
- Tadhunter, C. N., Villar-Martín, M., Morganti, R., Bland-Hawthorn, J., Axon, D., 2000, *MNRAS*, 314, 849
- Tingay, S. J., 1997, *A&A* 327, 550
- van Breugel, W. J. M., Fillipenko, A. V., Heckman, T. M., Miley, G. K., 1985, *ApJ*, 293, 83
- van Breugel, W., Miley, G., Heckman, T., Butcher, H., Bridle, A., 1985, *ApJ*, 290, 496
- Veilleux, S., Osterbrock, D. E., 1987, *ApJS*, 63, 295
- Villar-Martín, M., Tadhunter, C. N., Morganti, R., Axon, D., Koekemoer, A., 1999, *MNRAS*, 307, 24

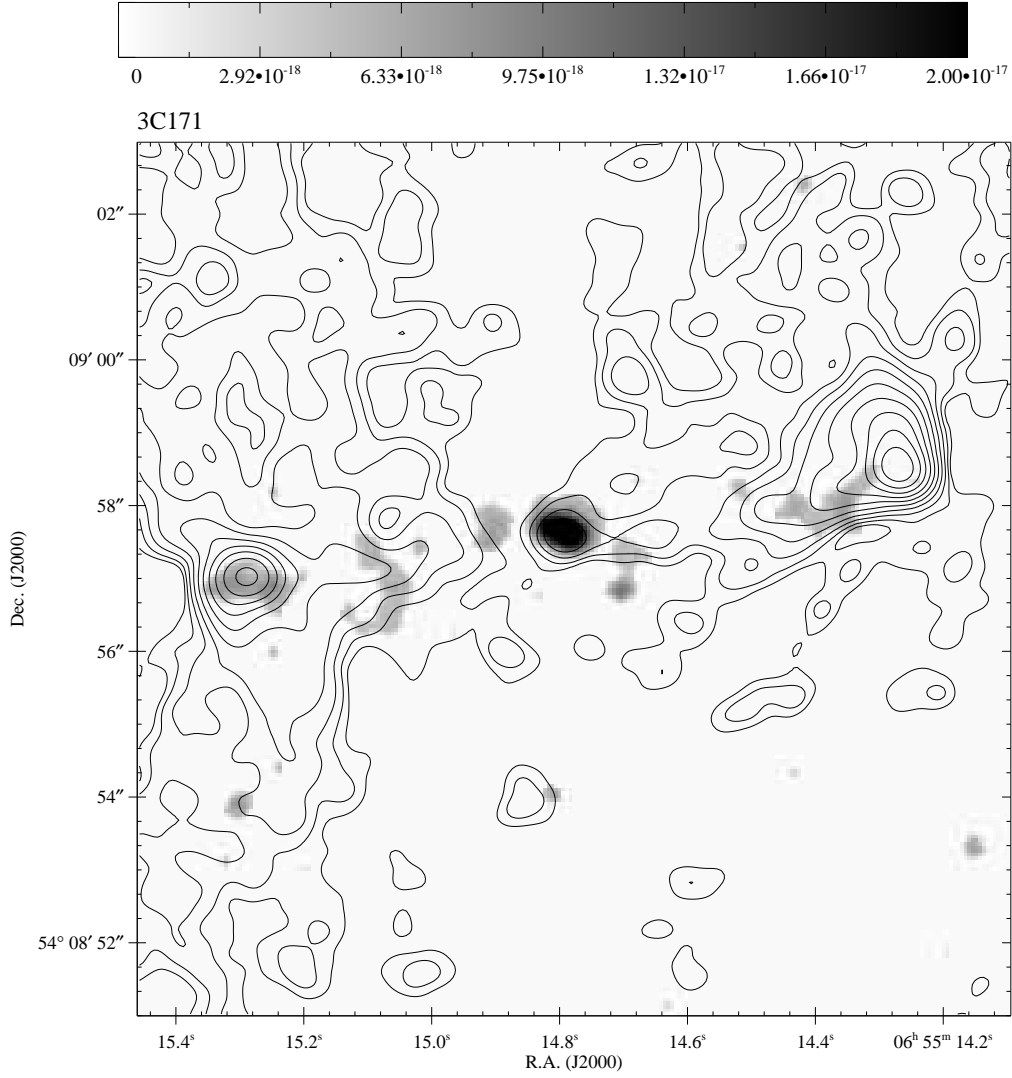


Fig. 1.— 3C171: Contour plot of radio image overlaid on gray-scale surface brightness plot of [OII] $\lambda$ 3727 emission line image. The [OII] image has been masked to retain emission above  $3.888 \times 10^{-18}$  ergs s<sup>-1</sup> cm<sup>-2</sup> arcsec<sup>-2</sup>. The 8 GHz VLA radio image is displayed with contour levels starting at 3 times the rms noise:  $3 \times 2.167 \times 10^{-5} \times [1, 2, 4, 8, 16, 32, 64, 128, 256, 512, 1024, 2048]$  Jy/beam.

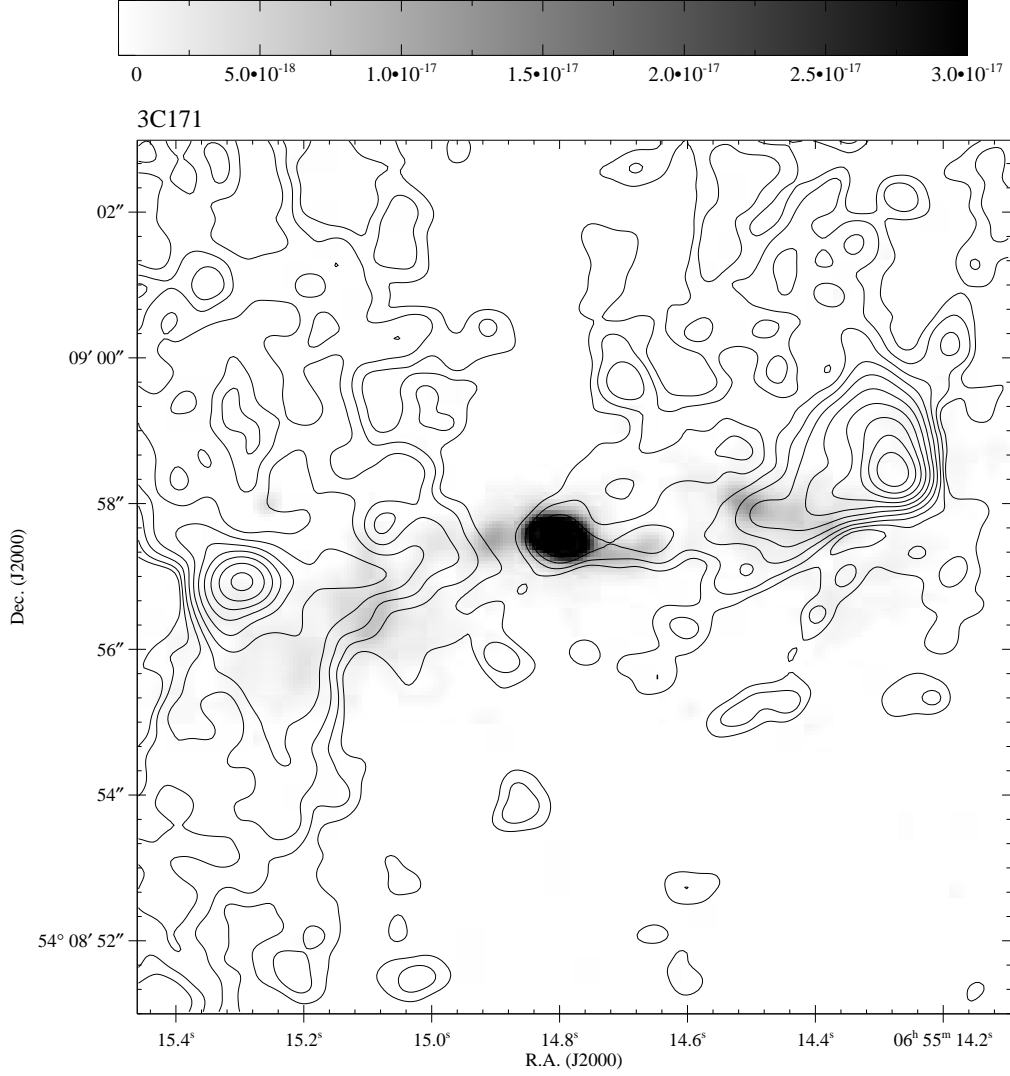


Fig. 2.— 3C171: Contour plot of radio image overlaid on gray-scale surface brightness plot of [OIII] $\lambda$ 5007 emission line image. The [OIII] image has been masked to retain emission above  $6.066 \times 10^{-19}$  ergs s $^{-1}$  cm $^{-2}$  arcsec $^{-2}$ . The 8 GHz VLA radio image is displayed with contour levels starting at 3 times the rms noise:  $3 \times 2.167 \times 10^{-5} \times [1, 2, 4, 8, 16, 32, 64, 128, 256, 512, 1024, 2048]$  Jy/beam.

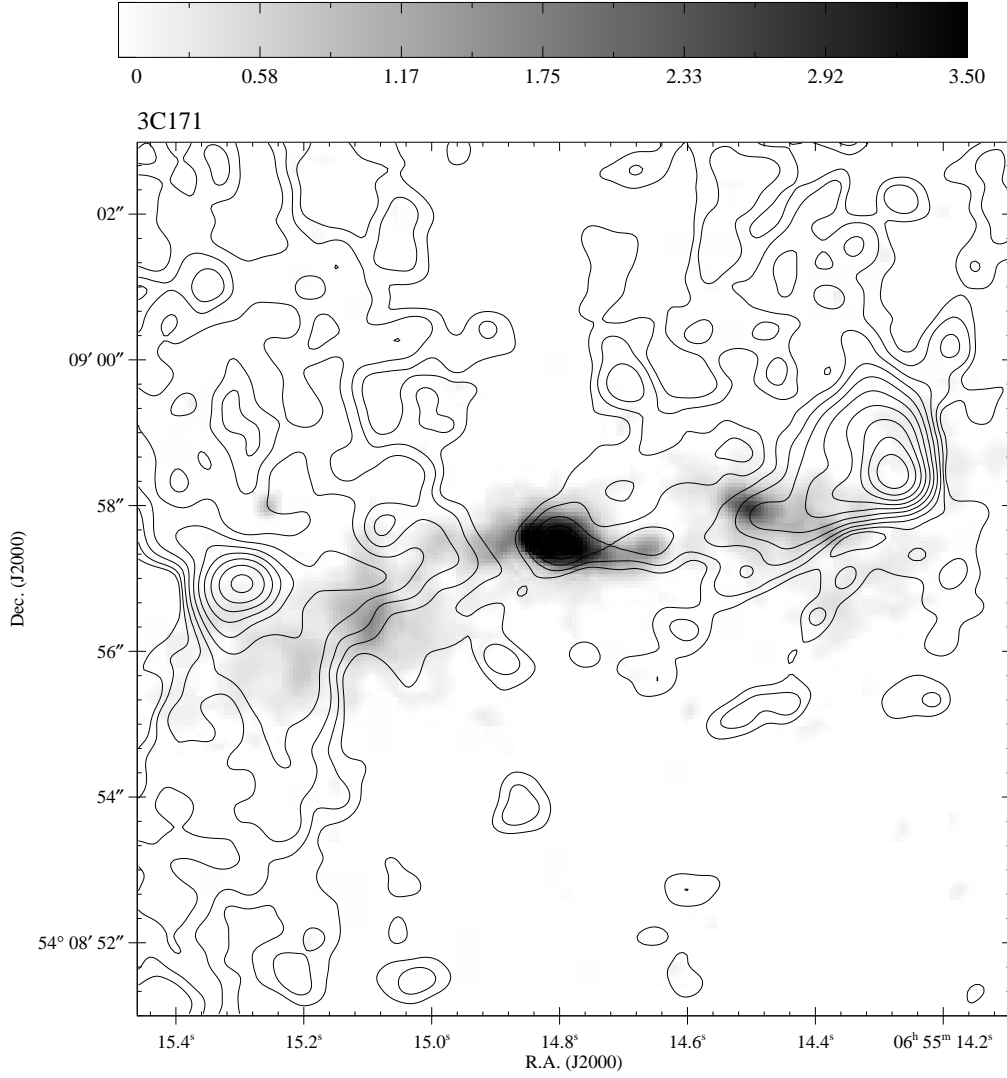


Fig. 3.— 3C171: Contour plot of radio image overlaid on gray-scale plot of the  $[\text{OIII}]\lambda 5007/[\text{OII}]\lambda 3727$  ratio image. Non-detections of  $[\text{OII}]$  are replaced with the  $3\sigma$  value to allow displays of lower limits to the ratio. The 8 GHz VLA radio image is displayed with contour levels starting at 3 times the rms noise:  $3 \times 2.167 \times 10^{-5} \times [1, 2, 4, 8, 16, 32, 64, 128, 256, 512, 1024, 2048] \text{ Jy/beam}$ .

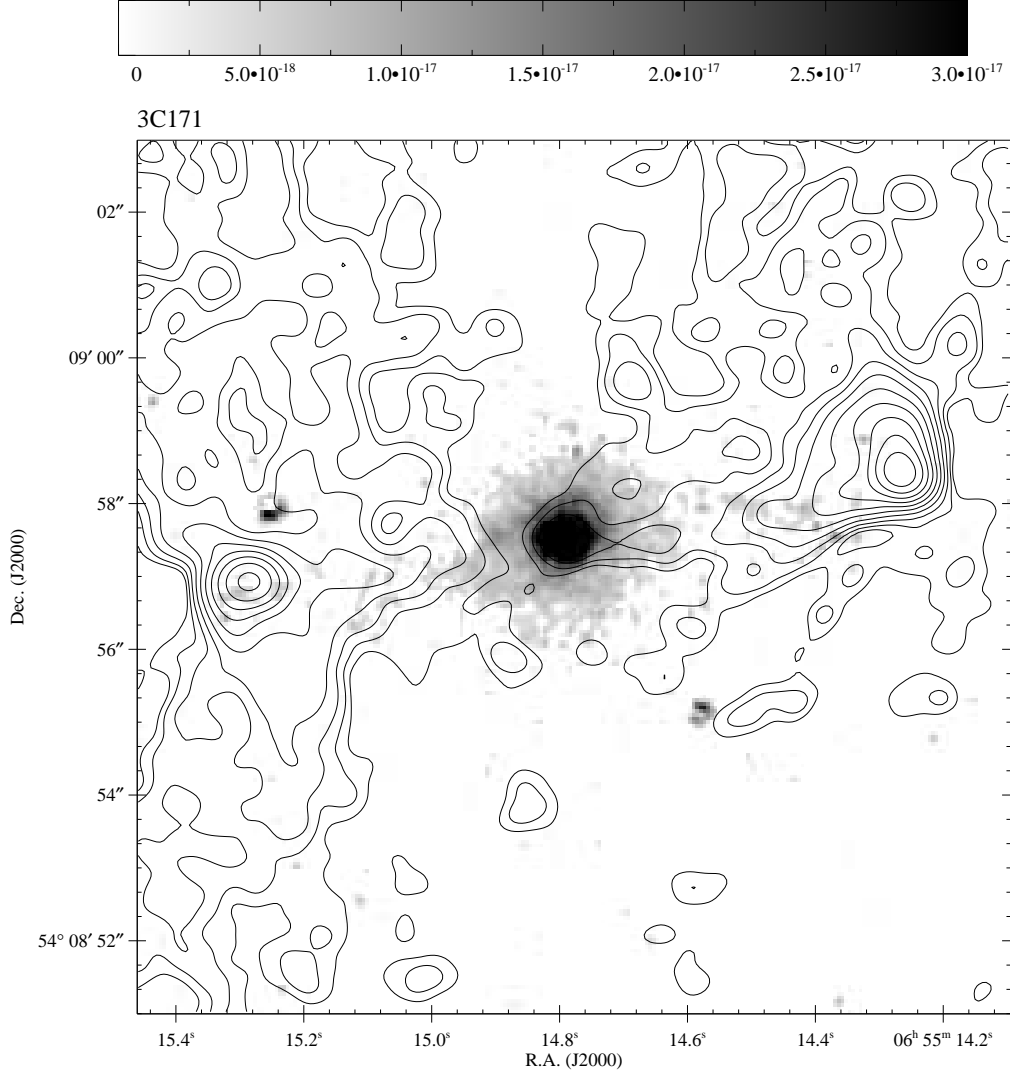


Fig. 4.— 3C171: Contour plot of radio image overlaid on gray-scale F547M continuum image. The continuum image has been masked to retain emission above  $3.651 \times 10^{-18}$  ergs s<sup>-1</sup> cm<sup>-2</sup> arcsec<sup>-2</sup>. The 8 GHz VLA radio image is displayed with contour levels starting at 3 times the rms noise:  $3 \times 2.167 \times 10^{-5} \times [1, 2, 4, 8, 16, 32, 64, 128, 256, 512, 1024, 2048]$  Jy/beam.

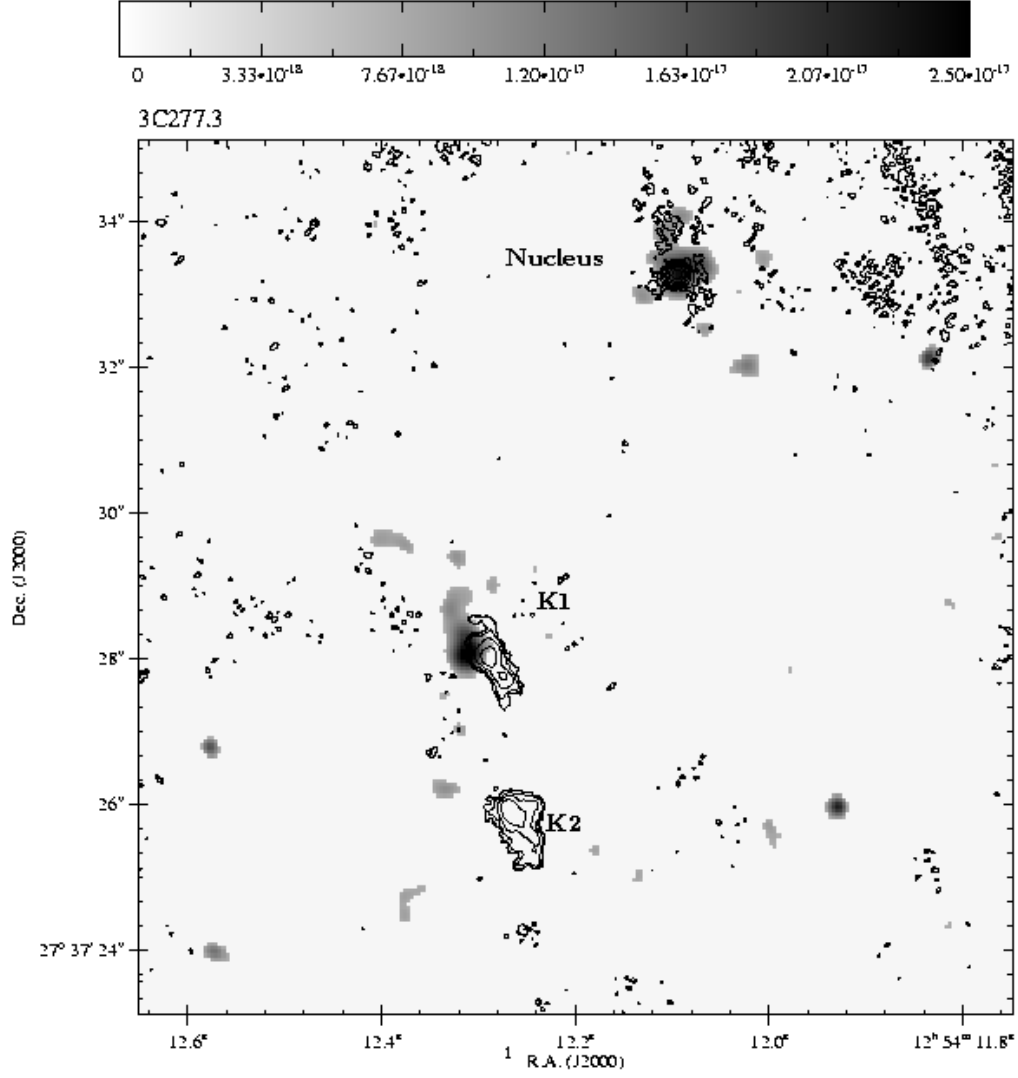


Fig. 5.— 3C277.3: Contour plots of radio image are overlaid on gray-scale surface brightness plot of [OII]λ3727 emission line image. The [OII] image has been masked to retain emission above  $7.332 \times 10^{-18}$  ergs s<sup>-1</sup> cm<sup>-2</sup> arcsec<sup>-2</sup>. The 4.8 GHz MERLIN2 + VLA radio image is displayed with contour levels starting at 3 times the rms noise:  $3 \times 1.608 \times 10^{-5} \times [1, 2, 4, 8, 16, 32, 64, 128, 256, 512, 1024, 2048]$  Jy/beam.

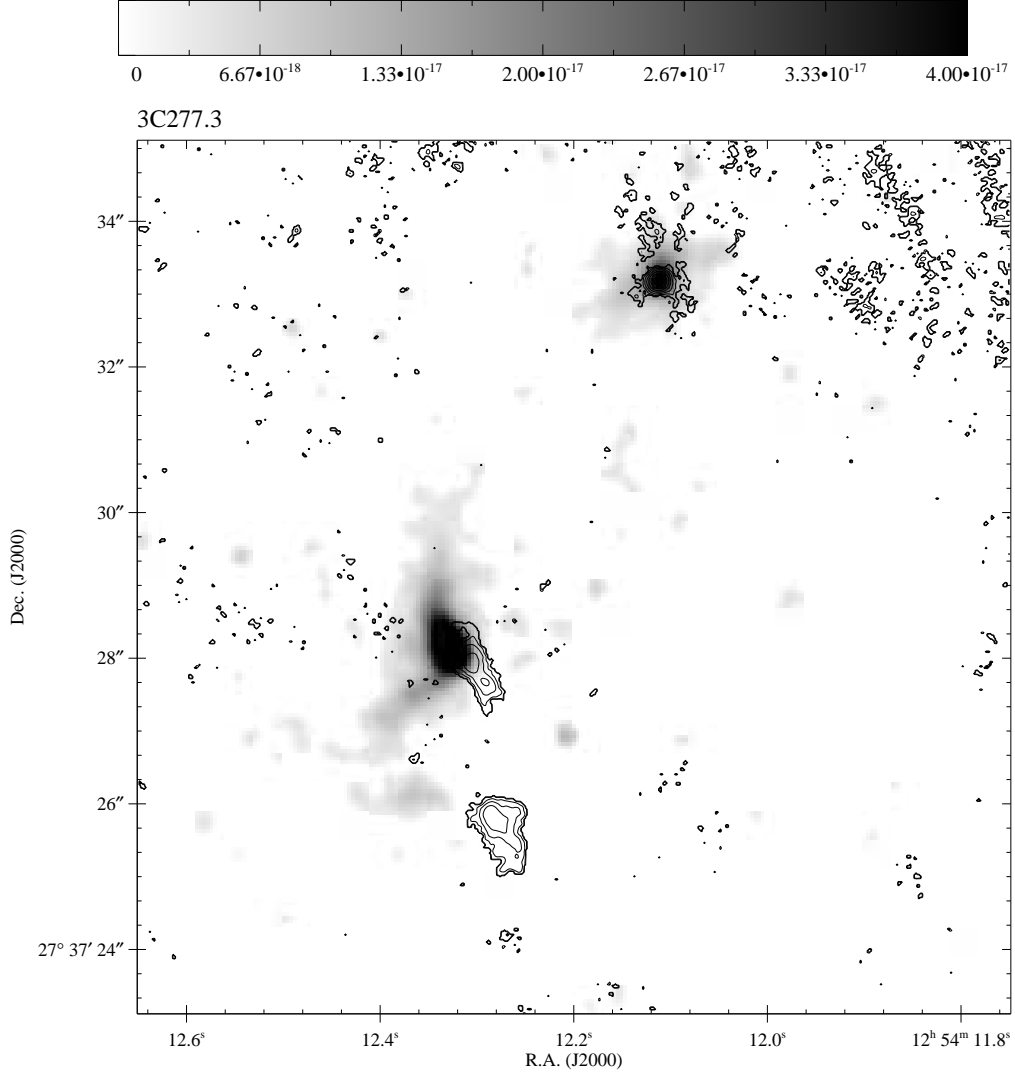


Fig. 6.— 3C277.3: Contour plots of radio image are overlaid on gray-scale surface brightness plot of  $[\text{OIII}]\lambda 5007$  emission line image. The  $[\text{OIII}]$  image has been masked to retain emission above  $1.033 \times 10^{-18} \text{ ergs s}^{-1} \text{ cm}^{-2} \text{ arcsec}^{-2}$ . The 4.8 GHz MERLIN2 + VLA radio image is displayed with contour levels starting at 3 times the rms noise:  $3 \times 1.608 \times 10^{-5} \times [1, 2, 4, 8, 16, 32, 64, 128, 256, 512, 1024, 2048] \text{ Jy/beam}$ .

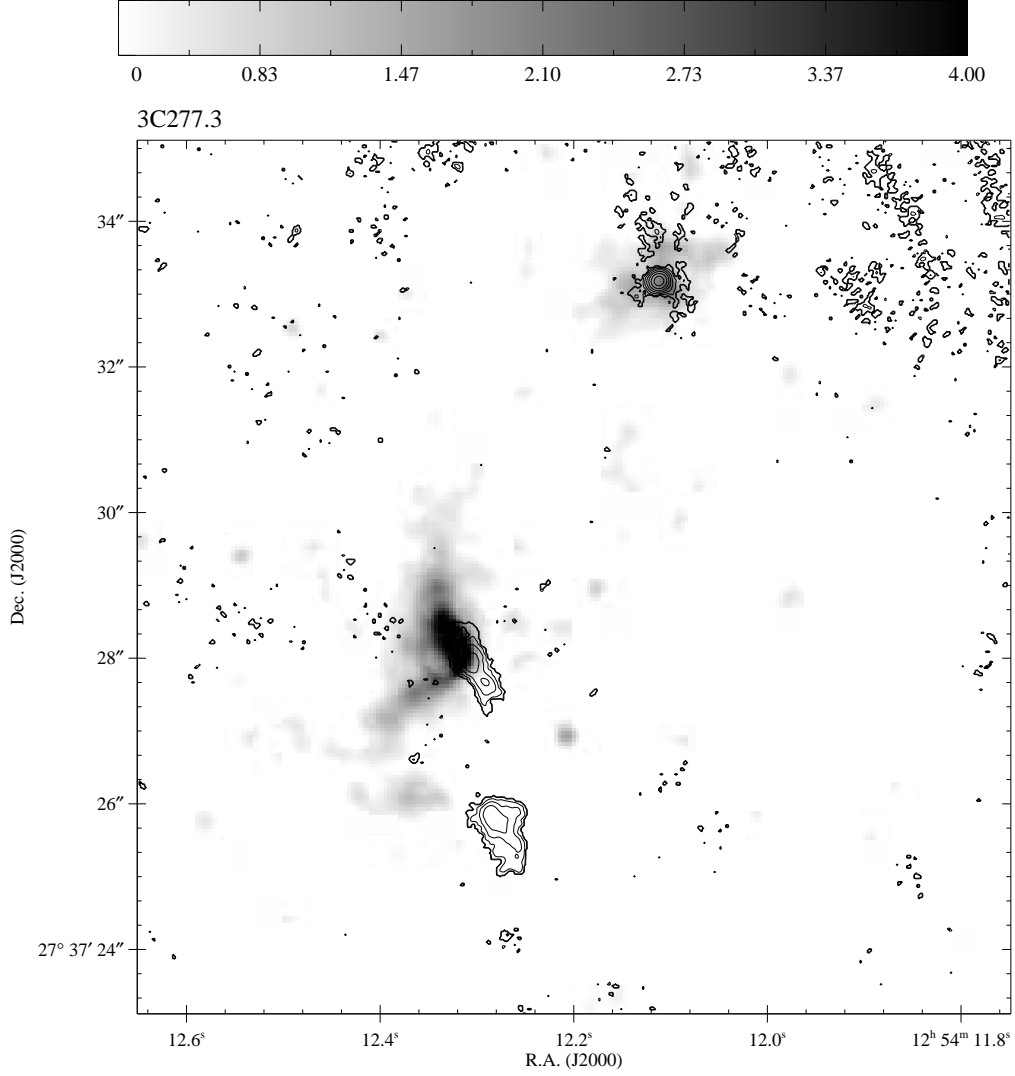


Fig. 7.— 3C277.3: Contour plot of radio image overlaid on gray-scale plot of the  $[\text{OIII}]\lambda 5007/[\text{OII}]\lambda 3727$  ratio image. Non-detections of  $[\text{OII}]$  are replaced with the  $3\sigma$  value to allow displays of lower limits to the ratio. The 4.8 GHz MERLIN2 + VLA radio image is displayed with contour levels starting at 3 times the rms noise:  $3 \times 1.608 \times 10^{-5} \times [1, 2, 4, 8, 16, 32, 64, 128, 256, 512, 1024, 2048] \text{Jy/beam}$ .

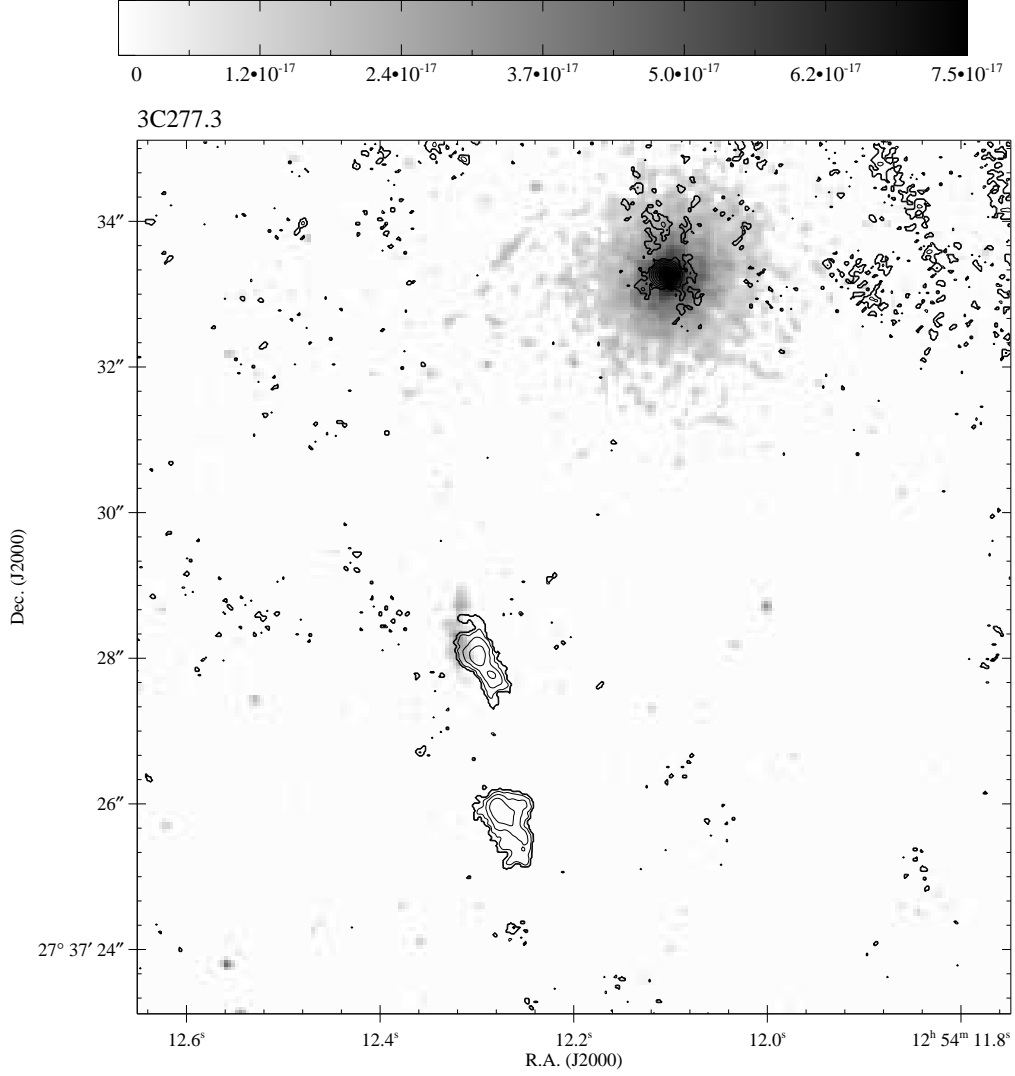


Fig. 8.— 3C277.3: Contour plots of radio image are overlaid on gray-scale F467M continuum image. The continuum image has been masked to retain emission above  $8.931 \times 10^{-18}$  ergs s<sup>-1</sup> cm<sup>-2</sup> arcsec<sup>-2</sup>. The 4.8 GHz MERLIN2 + VLA radio image is displayed with contour levels starting at 3 times the rms noise:  $3 \times 1.608 \times 10^{-5} \times [1, 2, 4, 8, 16, 32, 64, 128, 256, 512, 1024, 2048]$  Jy/beam.

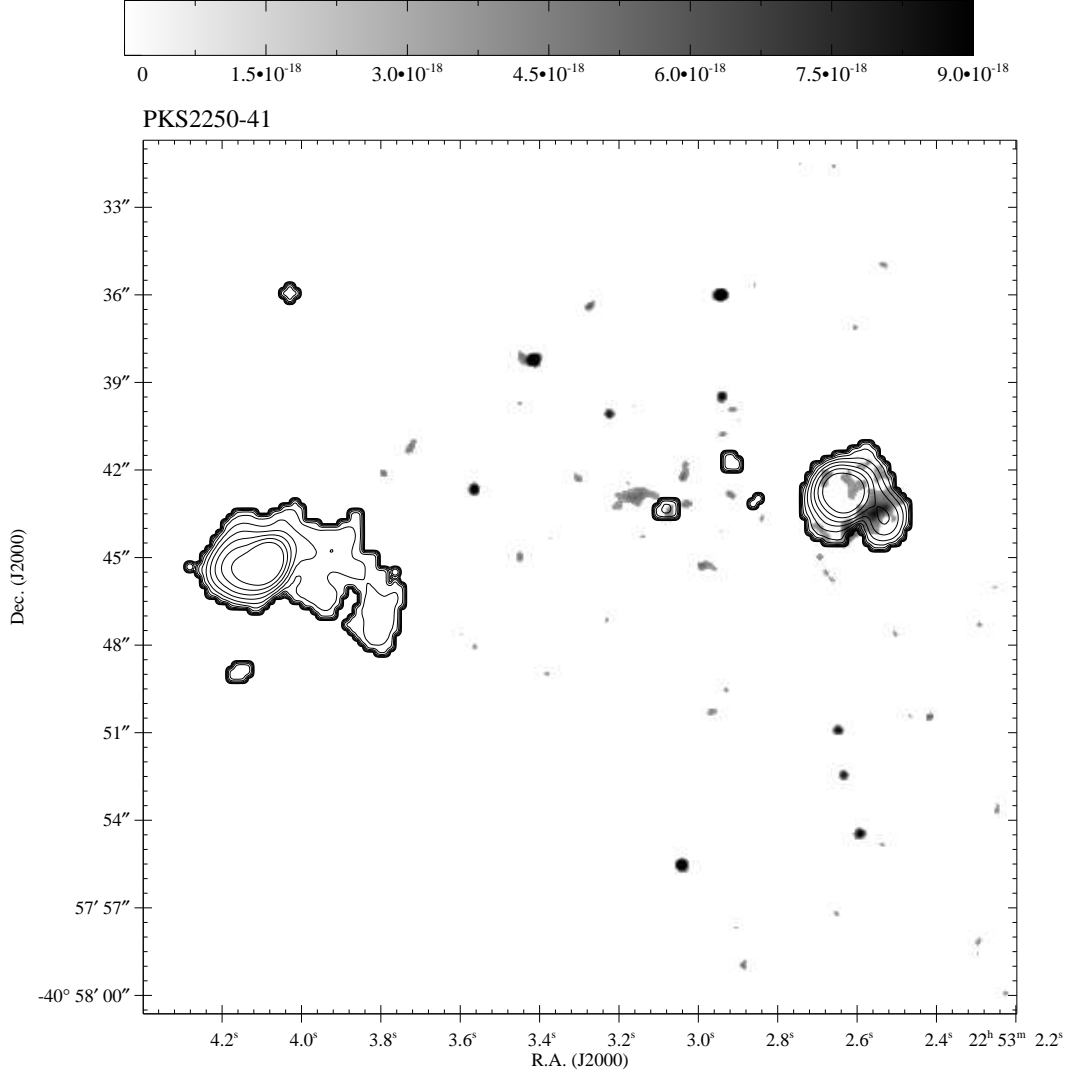


Fig. 9.— PKS2250-41: Contour plot of radio image overlaid on gray-scale surface brightness plot of [OII]λ3727 emission line image. The [OII] image has been masked to retain emission above  $3.156 \times 10^{-18} \text{ ergs s}^{-1} \text{cm}^{-2} \text{arcsec}^{-2}$ . The eastern lobe detected in the radio image is off the edge of the [OII] image. The 15 GHz VLA radio image is displayed with contour levels starting at 3 times the rms noise:  $3 \times 3.180 \times 10^{-6} \times [1, 2, 4, 8, 16, 32, 64, 128, 256, 512, 1024, 2048] \text{Jy/beam}$ .

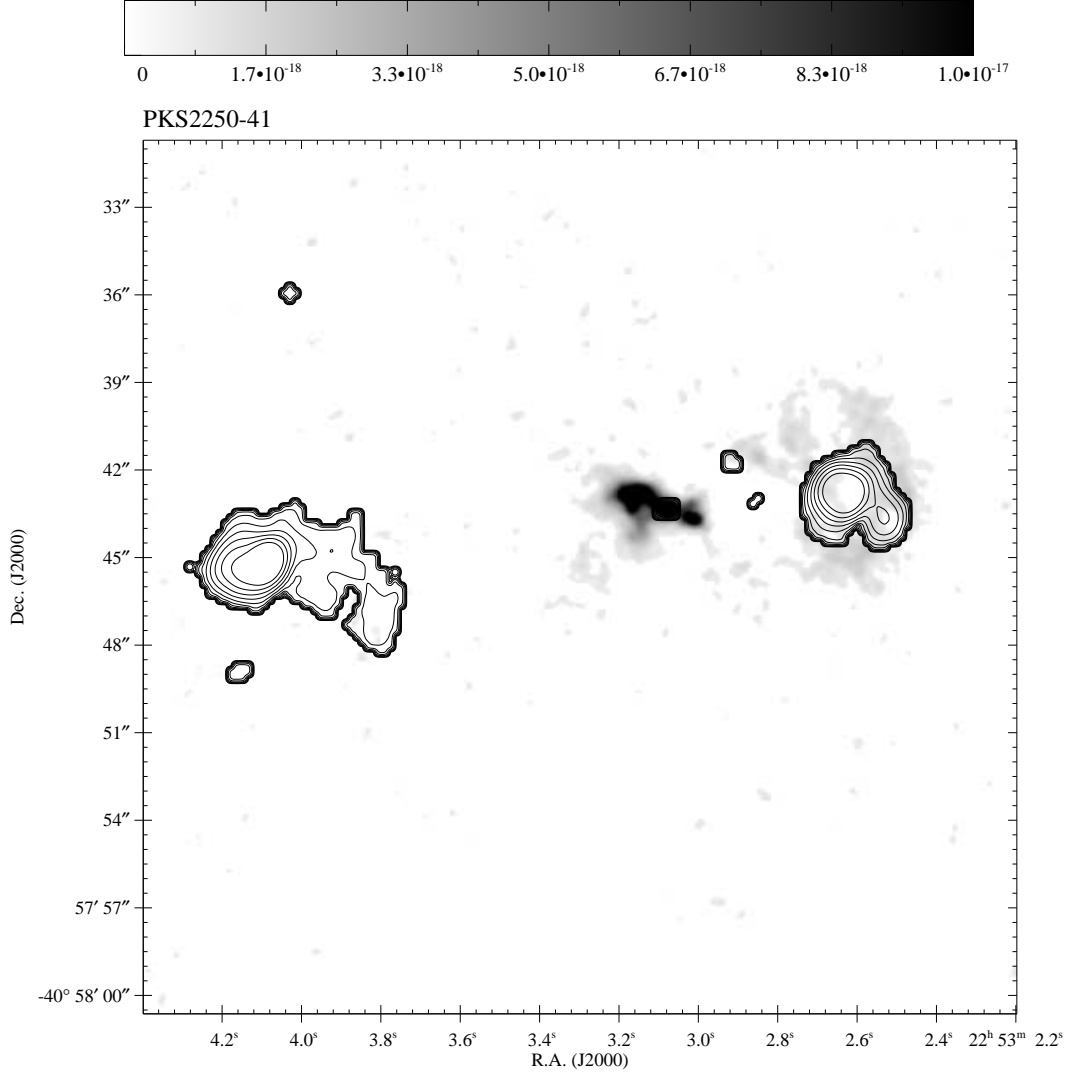


Fig. 10.— PKS2250-41: Contour plot of radio image overlaid on gray-scale surface brightness plot of [OIII]λ5007 emission line image. The [OIII] image has been masked to retain emission above  $6.657 \times 10^{-19} \text{ ergs s}^{-1} \text{cm}^{-2} \text{arcsec}^{-2}$ . The 15 GHz VLA radio image is displayed with contour levels starting at 3 times the rms noise:  $3 \times 3.180 \times 10^{-6} \times [1, 2, 4, 8, 16, 32, 64, 128, 256, 512, 1024, 2048] \text{ Jy/beam}$ .

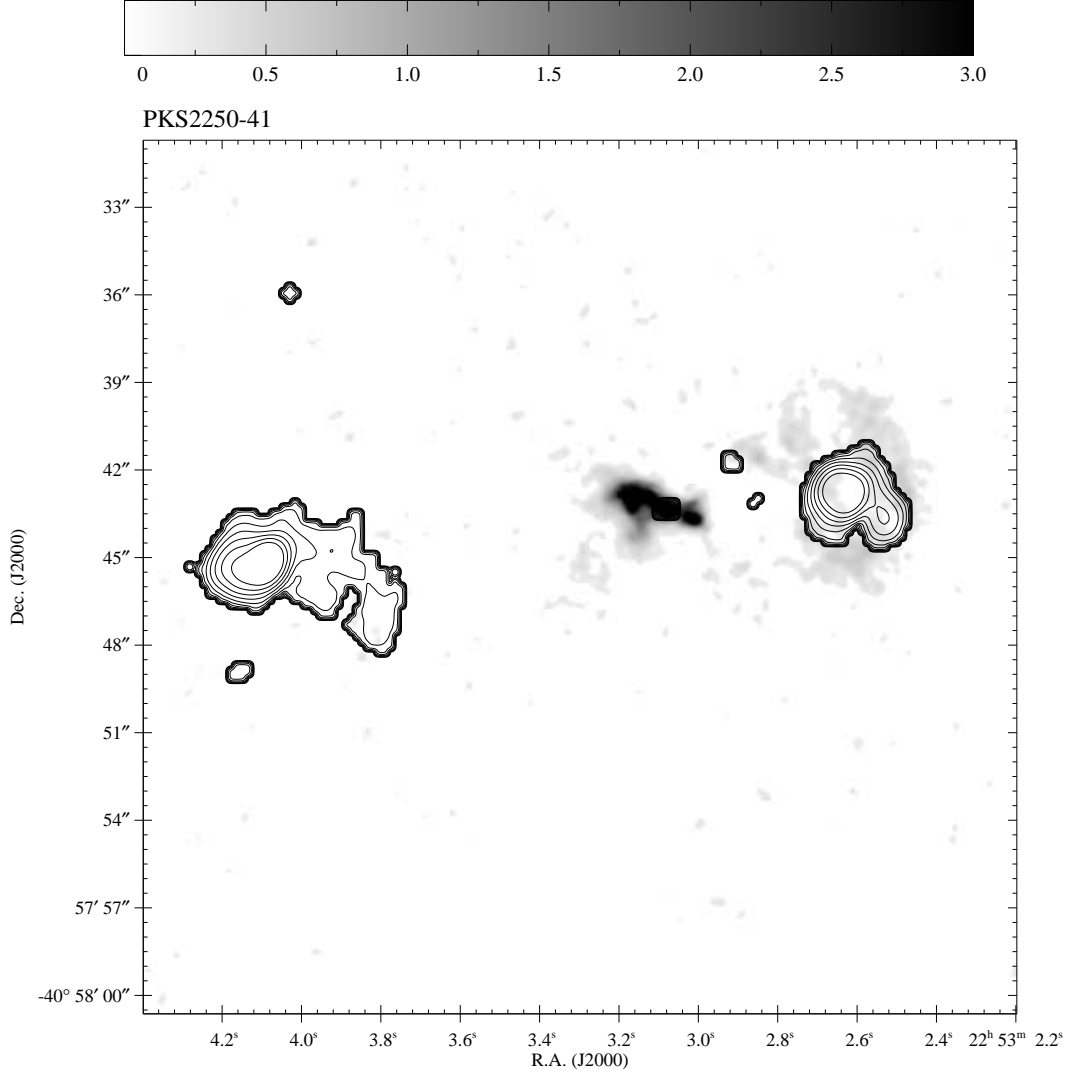


Fig. 11.— PKS2250-41: Contour plot of radio image was overlaid on gray-scale surface plot of the  $[\text{OIII}]\lambda 5007/[\text{OII}]\lambda 3727$  ratio image. Non-detections of  $[\text{OII}]$  are replaced with the  $3\sigma$  value to allow displays of lower limits to the ratio. The 15 GHz VLA radio image is displayed with contour levels starting at 3 times the rms noise:  $3 \times 3.180 \times 10^{-6} \times [1, 2, 4, 8, 16, 32, 64, 128, 256, 512, 1024, 2048] \text{ Jy/beam}$ .

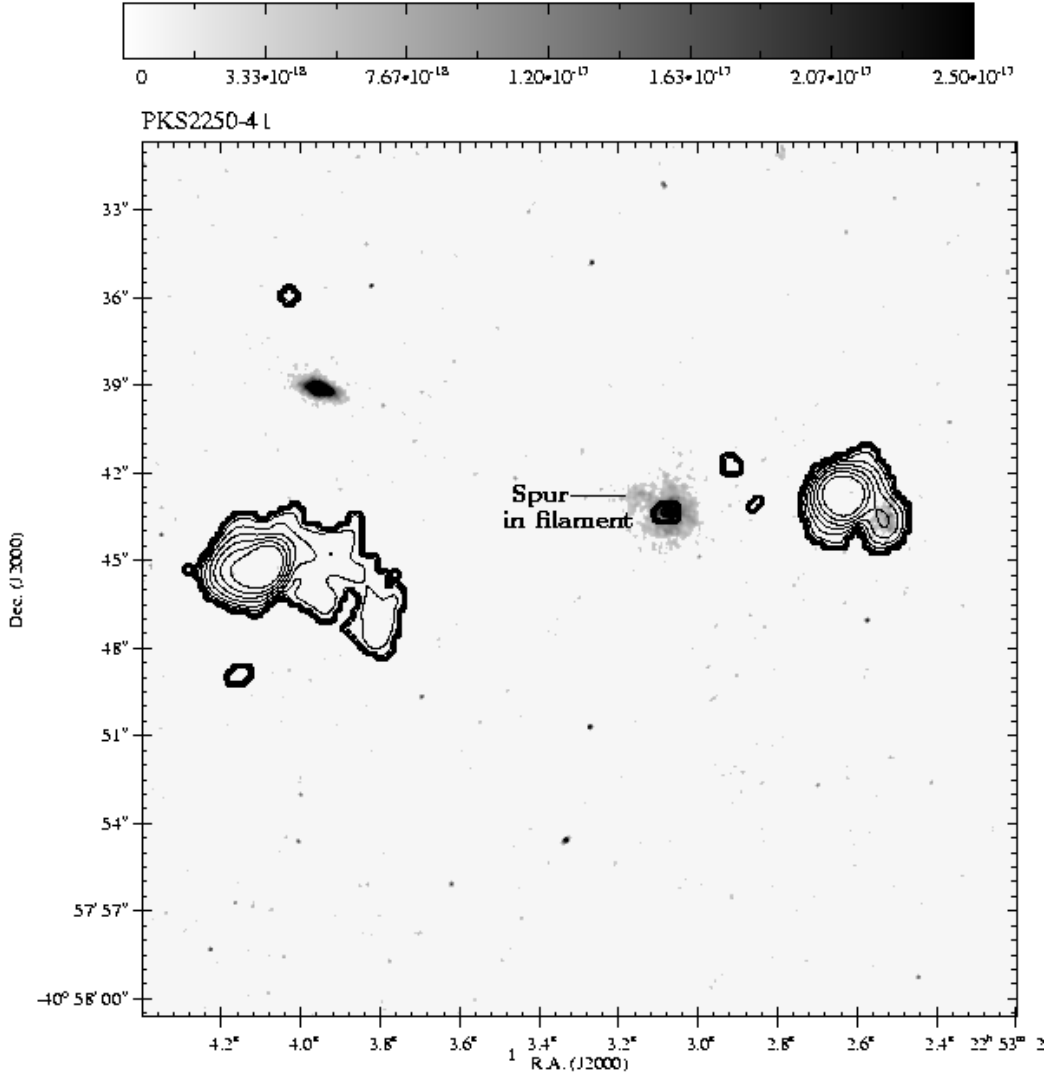


Fig. 12.— PKS2250-41: Contour plot of radio image overlaid on gray-scale F547M continuum image. The continuum image has been masked to retain emission above  $3.858 \times 10^{-18}$  ergs s<sup>-1</sup> cm<sup>-2</sup> arcsec<sup>-2</sup>. The 15 GHz VLA radio image is displayed with contour levels starting at 3 times the rms noise:  $3 \times 3.180 \times 10^{-6} \times [1, 2, 4, 8, 16, 32, 64, 128, 256, 512, 1024, 2048]$  Jy/beam.

Table 1. Properties of the galaxies

Object	RA(J2000)	DEC(J2000)	redshift <sup>a</sup>	Magnitude	E(B-V)	Applied correction <sup>c</sup>
(1)	h m s (2)	d m s (3)	(4)	mag (5)	mag (6)	(7)
3C171	06 51 14.8	+54 09 00	0.2384	18.89 <sup>1</sup>	0.40 <sup>b</sup>	0.87
3C277.3	12 54 11.7	+27 37 33	0.0857	15.94 <sup>1</sup>	0.012 <sup>a</sup>	0.99
PKS2250-41	22 53 03.1	−40 57 46	0.3100	20.0 <sup>2</sup>	0.14 <sup>b</sup>	0.95

<sup>1</sup>V band magnitude, from Spinrad *et al.* (1985)

<sup>2</sup>m<sub>p</sub> from Hunstead (1971)

<sup>a</sup>Obtained from NASA Extragalactic Database

<sup>b</sup>Determined using observed H $\alpha$ /H $\beta$  ratio (Clark *et al.* 1997; Clark *et al.* 1998)

<sup>c</sup>Total reddening correction using E(B-V) in Column (6) applied to the [OIII]/[OII] ratio image.

Table 2. Radio Properties

Object	Radio Power <sup>a</sup> ergs/s/Hz	Radio Luminosity ergs/s	Angular Size <sup>b</sup> arcsec	Linear Size kpc	Scale kpc/arcsec	Spectral Index
3C171	$5.18 \times 10^{33}$	$1.39 \times 10^{43}$	33 <sup>c</sup>	111.5	3.38	-0.94
3C277.3	$4.56 \times 10^{32}$	$1.14 \times 10^{41}$	40	58.8	1.47	-0.70
PKS2250-41	$2.75 \times 10^{33}$	$2.06 \times 10^{43}$	77	21.4	4.05	-0.99

Note. — The references for spectral index are 3C171: Clark *et al.* (1998); 3C277.3: van Breugel *et al.* (1985); PKS2250-41: Morganti *et al.* (1993).

<sup>a</sup>Corresponding frequency for 3C171 and 3C277.2 is 1.4GHz and for PKS2250-41 is 4.885GHz

<sup>b</sup>Refers to the maximum extension of the radio source

<sup>c</sup>Includes the diffuse plumes

Table 3. HST Optical images

Object	Emission Line	Chip	Filter	Date	Exposure Time sec	Mean $\lambda$ Å	Bandwidth Å
3C171	[OII]	3	FR418N	02/10/1999	2000	4615	60
	[OIII]	2	FR680P15	02/10/1999	3000	6195	81
	Continuum	2	F547M	02/10/1999	1000	5484	484
3C277.3	[OII]	3	FR418N18	08/01/1997	2000	4044	53
	[OIII]	4	FR533N	08/01/1997	1000	5436	71
	Continuum	2	F467M	08/01/1997	1000	4670	178
PKS2250-41	[OII]	3	FR533N	09/01/1999	2000	4862	63
	[OIII]	3	FR680N	09/01/1999	3000	6550	85
	Continuum	2	F547M	09/01/1999	1000	5484	484

Note. — The pixel scale for Chip 2 is 0.9961 arcsec/pixel, for chip 3 is 0.9958 arcsec/pixel and for chip 4 is 0.9964 arcsec/pixel. The observations are from program 6657. The bandwidth for the LRF images is  $\sim 1.3\%$  of the central wavelength.

Table 4. Properties : Radio images

Object	Telescope	Date	Integration time	Frequency	Bandwidth	rms mJy/beam	Clean Beam
3C171	VLA	08/06/1995	3550s	8 GHz	50 MHz	0.044	$0.35'' \times 0.25''$ PA= 75 deg
3C277.3	VLA <sup>a</sup>	06/10/1982	680s	5 GHz	50 MHz		
3C277.3	Merlin2	03/04/2000	36 hrs	5 GHz	15 MHz	0.043 <sup>b</sup>	$0.15'' \times 0.15''$
PKS2250-41	VLA	09/17/1995	5210s	15 GHz	50 MHz	0.090	$0.82'' \times 0.33''$ PA= −11.4 deg

<sup>a</sup>VLA archive data from J. Ekers(1982).

<sup>b</sup>Combined MERLIN2 and VLA data.

Table 5. Properties : Position angles in PKS 2250-41

Object	Feature	Emission	Position Angle (degrees)
Companion	Orientation vector <sup>a</sup>	Continuum	71
Companion	Major axis	Continuum	69
PKS2250-41	1'' Spur in Filament	Continuum	63
PKS2250-41	Filament	[OIII]	67

<sup>a</sup>A line joining nuclei of the companion and PKS2250-41

Table 6.  $[\text{OIII}]/[\text{OII}]$  Values in Selected Regions

Object (1)	Region (2)	Observed Ratio (3)
3C171	Nucleus	$3.9 \pm 0.6^{\text{a}}$
	Eastern lobe	$1.6 \pm 0.2$
	Eastern hotspot	$> 0.4^{\text{b}}$
	Western lobe	$2.7 \pm 0.4$
	Western hotspot	$> 0.3^{\text{b}}$
3C277.3	Nucleus	$2.0 \pm 0.3$
	Knot K <sub>1</sub>	$7.0 \pm 1.0$
	1'' E of Knot K <sub>2</sub>	$1.2 \pm 0.2^{\text{c}}$
PKS2250-41	Nucleus	$3.9 \pm 0.6$
	Filament	$5.7 \pm 0.8$
	Western hotspot	$0.7 \pm 0.1$

Note. — Column 3 gives the maximum observed values for the  $[\text{OIII}]/[\text{OII}]$  ratio in various regions of the galaxies when both  $[\text{OIII}]$  and  $[\text{OII}]$  are detected with  $S/N \gtrsim 3$ .

<sup>a</sup>The uncertainty has been calculated by propagating the uncertainties associated with data analysis and photometric calibration through all the steps in the analysis.

<sup>b</sup>There are regions near the hot spots in 3C171 where the  $[\text{OII}]$  and  $[\text{OIII}]$  emission does not overlap. However we do detect  $[\text{OIII}]$  emission near both hotspots and  $[\text{OII}]$  at the Eastern hot spot. The ratios quoted are for regions near the hotspots with significant  $[\text{OIII}]$  emission but little or no  $[\text{OII}]$  emission and are the lower limit given by setting  $[\text{OII}]$  to the  $3\sigma$  value.

<sup>c</sup>Here the quoted value for the ratio corresponds to emission 1'' East of K2.